ACS APPLIED MATERIALS & INTERFACES

Research Article

www.acsami.org

Evaluation of Dysprosia Aerogels as Drug Delivery Systems: A Comparative Study with Random and Ordered Mesoporous Silicas

Abhishek Bang,[†] Anand G. Sadekar,[†] Clayton Buback,[†] Brice Curtin,[†] Selin Acar,[†] Damir Kolasinac,[‡] Wei Yin,[§] David A. Rubenstein,[§] Hongbing Lu,[∥] Nicholas Leventis,*[,†] and Chariklia Sotiriou-Leventis*[,†]

[†]Department of Chemistry, Missouri University of Science and Technology, Rolla, Missouri 65409, United States

[‡]School of Mechanical and Aerospace Engineering, Oklahoma State University, Stillwater, Oklahoma 74078, United States

[§]Department of Biomedical Engineering, Stony Brook University, Stony Brook, New York 11794, United States

[∥]Department of Mechanical Engineering, University of Texas at Dallas, Richardson, Texas 75080, United States

Supporting Information

ABSTRACT: Biocompatible dysprosia aerogels were synthesized from $DyCl_3 \cdot 6H_2O$ and were reinforced mechanically with a conformal nano-thin-polyurea coating applied over their skeletal framework. The random mesoporous space of dysprosia aerogels was filled up to about 30% v/v with paracetamol, indomethacin, or insulin, and the drug release rate was monitored spectrophotometrically in phosphate buffer (pH = 7.4) or 0.1 M aqueous HCl. The drug uptake and release study was conducted comparatively with polyurea-crosslinked random silica aerogels, as well as with as-prepared (native) and polyurea-crosslinked mesoporous silica perforated with ordered 7 nm tubes in hexagonal packing. Drug uptake from random nanostructures (silica or dysprosia) was higher (30−35% w/w) and the release rate was slower (typically >20 h) relative to ordered silica (19−21% w/w, <1.5 h, respectively). Drug release data from dysprosia aerogels were fitted with a flux equation consisting of three additive terms that correspond to drug stored successively in three hierarchical pore sites on the skeletal framework. The high drug uptake and slow release from dysprosia aerogels, in combination with their low toxicity, strong paramagnetism, and the possibility for neutron activation render those materials attractive multifunctional vehicles for site-specific drug delivery.

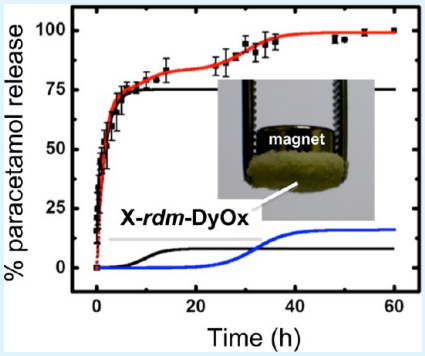

KEYWORDS: *rare earth, dysprosium, aerogels, drug delivery, biocompatibility, paracetamol, indomethacin, insulin*

1. INTRODUCTION

Current research on drug delivery is focusing on improving pharmacokinetic and pharmacodynamic properties, including controlled drug release, long residence time, and biocompatibility.[1−3] From that perspective, nanotechnology may play a pivotal role in the development of complex multifunctional drug delivery systems[4] that may prove more effective than conventional methods in terms of both site-specific delivery and protection against enzymatic degradation.[5] Liposome-based drug delivery systems were the first to gain FDA approval.[6] Subsequently, carbon-[7,8] and gold-based[9] nanomaterials, hydrogels,[10,11] dendrimers,[12,13] polymer nanoparticles,[14] and magnetic nanoparticles,[15,16] have all emerged as potential drug delivery systems. In that regard, aerogels as a class of highly porous, low-density nanostructured materials with large pore volumes (typically >90%) and very large surface-to-volume ratios,[17] are also gaining significant attention as hosts for pharmaceuticals in drug delivery.[18,19]

The most common type of aerogels is based on silica, and comes in two main varieties: with ordered,[20−22] or random[23] mesoporosity (pore sizes in the 2−50 nm range). The relative advantages of the two types have been debated,[24] but both kinds have been investigated as drug delivery systems. Ordered mesoporous silica is perforated with a periodic array of hexagonal tubes with uniform size, which have been considered desirable for storing the active substance.[25,26] In random silica, drug is adsorbed on the surfaces that define their mesoporous space. Ordered mesoporous silica offers the possibility to control release with photo,[27−29] heat,[30] pH,[31−33] or magnetically[34,35] responsive caps over the hexagonal tubes. Random mesoporous silica offers fast drug release, although controllable release has been described by surface modification.[36−38] The main overall disadvantage of silica, however, has been its toxicity.[39] Under physiological conditions (phosphate buffer saline), silica aerogels can undergo degradation to silicic acid, which in turn can nucleate causing adverse effects because of accumulation of fine particles in the body.[40] Biocompatibility is enhanced either by surface functionalization with small biocompatible organic molecules, or by coating with biocompatible polymers.[41,42] Along those lines, a current trend is to move away from silica altogether, into biocompatible/biodegradable polymer-based aerogels (e.g., starch, alginate, polysaccharides, etc.)[43−45] Another alternative would be to work with non-toxic metal oxide aerogels in combination with biocompatible polymer coatings.

Received: December 23, 2013
Accepted: March 13, 2014
Published: March 25, 2014

   dx.doi.org/10.1021/am4059217 | ACS Appl. Mater. Interfaces 2014, 6, 4891−4902

In that regard, dysprosium is a rare earth, which, despite its name (in Greek "difficult-to-get-to"), is quite abundant and inexpensive, and most importantly, its oxide (dysprosia) is practically insoluble and non-toxic.[46] Like all oxide aerogels, dysprosia aerogels (DyOx) consist of a network of nanoparticles and are fragile materials.[47] That issue has been addressed by coating the entire nanostructure with a nano-thin conformal polymer layer that reacts chemically and bridges covalently skeletal nanoparticles.[47] The resulting materials are referred to as polymer-crosslinked (X-) dysprosia aerogels, and for the purposes of this report are abbreviated as X-*rdm*-DyOx. It is also noted that polymer crosslinking not only improves the mechanical integrity of dysprosia aerogels but also combines an inherently non-toxic material with a polymer coating that potentially improves its biocompatibility even further by preventing peptization that would release colloidal nanoparticles that may present size-related toxicity.[48,49] (In that regard, it has been observed that all rare earth aerogels (from Sc to Lu)[47] are peptized in water.)

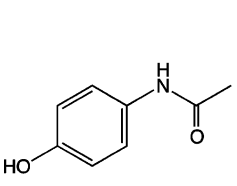

paracetamol

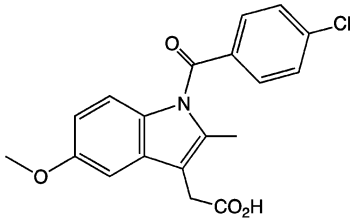

indomethacin

The potential of X-*rdm*-DyOx aerogels as drug delivery carriers was investigated with paracetamol (also referred to as acetaminophen, an analgetic and antipyretic drug), indomethacin (a non-steroidal anti-inflammatory drug), and insulin (a medium molecular weight peptide hormone (5808 Da) that regulates carbohydrate and fat metabolism). The study of X-*rdm*-DyOx was benchmarked against: (a) typical randomly mesoporous polymer-crosslinked silica (X-*rdm*-SiOx) aerogels;[50,51] (b) as-prepared (referred to as native) ordered mesoporous silica (n-*ord*-SiOx, that is, the kind perforated with hexagonal tubes);[52,53] and (c) polymer-crosslinked ordered mesoporous silica (X-*ord*-SiOx).[52,53] Materials characterization starts with a comparative biocompatibility study of X-*rdm*-DyOx aerogels and concludes with a correlation of the drug-release profile with the porous structure. In agreement with Rolison's conjecture on "the importance of nothing and the unimportance of periodicity,"[24] random nanoporous materials (silica as well as dysprosia) store more drug and release it slower than their ordered counterparts. By comparison to silica, however, in addition to its lower toxicity, dysprosia is also strongly paramagnetic, thereby is attracted by magnets just like iron fillings.[54,55] That property could be useful for focused drug delivery.[56] Also, dysprosium can become a beta radiation emitter by neutron activation.[57,58] Therefore, X-*rdm*-DyOx may be promising as multifunctional materials able to deliver simultaneously chemotherapy and radiation in targeted sites for the treatment of several ailments (cancer,[59,60] rheumatoid arthiritis[61,62]), comprising an effective, cost-efficient alternative to currently used surgical synovectomy.[63,64]

2. EXPERIMENTAL SECTION

2.1. Materials. All reagents and solvents were used as received unless noted otherwise. Pluronic P123 (a tri-block co-polymer of polyethylene oxide and polypropylene oxide: $PEO_{20}PPO_{70}PEO_{20}$), HNO_3, 2,4,6-trimethylbenzene (TMB), tetramethylorthosilicate (TMOS), 3-aminopropyltriethoxysilane (APTES), dysprosium(III) chloride hexahydrate ($DyCl_3.6H_2O$), epichlorohydrin (ECH), *N*-4-(hydroxyphenyl)-acetamide (paracetamol), 2-(1-(4-chlorobenzoyl)-5-methoxy-2-methyl-1*H*-indol-3-yl)acetic acid (indomethacin) and insulin from bovine pancreas (catalog no. I5500) were purchased from Sigma-Aldrich and were used without further purification. Desmodur N3200 is a high-viscosity, non-volatile diisocyanate derivative of 1,6-hexamethylene diisocyanate and was obtained courtesy of Bayer Corp. U.S.A. (A comprehensive chemical/spectroscopic characterization of Desmodur N3200 is given in the Supporting Information section of ref 65). HPLC grade ethanol, acetonitrile and acetone were purchased from Fisher Scientific. Siphon grade CO_2 was purchased from Ozarc Gas Co.

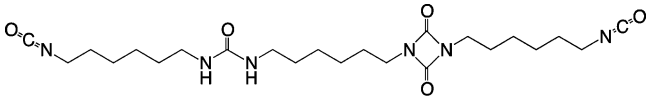

Desmodur N3200 diisocyanate

2.1.1. Polymer Cross-Linked Dysprosia Aerogels (X-rdm-DyOx). Polymer cross-linked dysprosia aerogels (X-*rdm*-DyOx) were synthesized via a modification of the previously described method.[47] A flow-chart of the procedure is given in Scheme S.1 of the Supporting Information. In brief, $DyCl_3{\cdot}6H_2O$ (2.64 g, 7.00 mmol) was dissolved in absolute ethanol (20 mL). Epichlorohydrin (5.49 mL, 70.0 mmol) was added to form the sol, which was poured into molds (Wheaton Polypropylene Omni-Vials, 1 cm in diameter, Part No. 225402). Gelation was observed in 10−12 min. Gels were aged in the molds for 3−4 days, and the pore-filling solvent was exchanged first with ethanol and then with acetone (8 h, 4×, respectively). Subsequently, wet-gels were cross-linked by first equilibrating with a solution of Desmodur N3200 (11 g) in acetone (94 mL) for 36 h at room temperature (RT), followed by heating at 60 °C for 3 days. X-linked wet-gels were washed with acetone (8 h, 4×), and were dried in an autoclave with liquid CO_2 taken out at the end as a supercritical fluid (SCF).

2.1.2. Ordered Native and Polymer Cross-Linked Mesoporous Silica Aerogels (n-ord-SiOx and X-ord-SiOx, Respectively). Ordered native and polymer cross-linked mesoporous silica aerogels (n-*ord*-SiOx and X-*ord*-SiOx, respectively) were synthesized via a modification of Nakanishi's method[66] as described previously.[52,53] A flow-chart of the procedure is given in Scheme S.2 of the Supporting Information. In brief, Pluronic P123 (4 g) was dissolved in 1.0 M aqueous HNO_3 (12 g) and the resulting solution was stirred overnight at room temperature (RT). TMB (0.45 g) was added and the mixture was stirred further for 30 min at RT. The mixture was cooled to 0 °C, TMOS (5.15 g) was added, and stirring was continued for another 30 min. The resulting sol was poured into molds as above and was kept at 60 °C for 12 h. The resulting wet-gels were washed with ethanol (8 h, 2×), followed by soxhlet extraction with acetonitrile for 3 days. Subsequently, wet-gels were washed with acetone (8 h, 4×) and were dried in an autoclave with liquid CO_2 taken out at the end as supercritical fluid (SCF) to obtain n-*ord*-SiOx aerogels. For X-*ord*-SiOx aerogels, ready-for-drying wet-gels were transferred instead into a solution of Desmodur N3200 (11 g) in acetone (94 mL) and were allowed to equilibrate for 36 h. Then, wet-gels submerged in their cross-linking solution were placed in an oven at 60 °C, followed by solvent exchange with acetone (4×, 8 h each time) and drying with SCF CO_2.

2.1.3. Cross-Linked Random-Silica Aerogels (X-rdm-SiOx). Cross-linked random-silica aerogels (X-*rdm*-SiOx) were synthesized as summarized in Scheme S.3 of the Supporting Information.[50,51] In brief, solution A consisting of TMOS (2.90 mL, 19.6 mmol), APTES (0.96 mL, 4.10 mmol), and CH_3CN (4.5 mL) was cooled at −78 °C and was mixed rapidly with solution B, also cooled at −78 °C, consisting of CH_3CN and H_2O (4.5 and 1.5 mL, respectively). The resulting sol was poured into molds as above to gel. Wet-gels were washed with CH_3CN (8 h, 4×), were transferred in a solution of Desmodur N3200 (11 g) in CH_3CN (94 mL) and were allowed to equilibrate for 36 h. Wet-gels were kept at 60 °C for 3 days; subsequently, they were washed with CH_3CN (8 h, 4×) and were dried in an autoclave with liquid CO_2 taken out at the end as a SCF.

2.2. Methods. Drying with SCF CO_2 was conducted in an autoclave (SPI-DRY Jumbo Critical Point Dryer, SPI Supplies, Inc. West Chester, PA). Bulk densities (ρ_b) were calculated from the weight and the physical dimensions of the samples. Surface areas, pore volumes and pore size distributions were measured with N_2 sorption porosimetry, using a Micromeritics ASAP 2020 surface area and porosity analyzer. Skeletal densities (ρ_s) were determined with helium pycnometry, using a Micromeritics AccuPyc II 1340 instrument. Percent porosities (Π) were determined via $\Pi = 100 \times [\rho_s - \rho_b)]/\rho_s$. Thermogravimetric analysis (TGA) was conducted in air with a TA Instruments Model TGA Q50 Thermogravimetric Analyzer at 10 °C min^{-1}; scanning electron microscopy (SEM) was conducted with Au/Pd coated samples on a Hitachi Model S-4700 field-emission microscope; transmission electron microscopy (TEM) was conducted with a FEI Technai F20 instrument employing a Schottky field emission filament operating at a 200 KV accelerating voltage. Absorbance was measured with a Cary 50 Bio UV−vis spectrophotometer.

2.3. Biocompatibility. *2.3.1. Hemolysis Testing.* X-*rdm*-DyOx aerogel samples (1 mg) were incubated with fresh human whole blood (30 μL, Oklahoma Blood Institute, Oklahoma City, OK) for 24 h at room temperature. Subsequently, blood samples were centrifuged at 1,000 g for 5 min, and the plasma was collected and diluted in substrate reagent provided with a hemoglobin measurement kit (C462-A, Catachem Inc., Oxford, CT), following manufacturer's instructions. Activator reagent (H_2O_2, 200 μL) was added so that hemoglobin in the samples could activate the substrate reagent and change the substrate color. The plasma hemoglobin concentration was determined by measuring the light absorbance of the substrate reagent at 600 nm.[67]

2.3.2. Aggregation Testing. Fresh human platelet rich plasma (PRP) samples (from Oklahoma Blood Institute) were diluted in autologous platelet poor plasma (PPP) to achieve a final platelet concentration of 250,000/μL. X-*rdm*-DyOx aerogel discs (1 mg) were incubated with that plasma (50 μL) for up to 24 h at RT. Aggregation toward $TRAP_6$ (thrombin receptor activator peptides, SFLLRN, 20 μM, Sigma Aldrich, St. Louis, MO) was conducted at 37 °C on timed PRP samples at 0, 2, 4, 6, and 24 h using a Chrono-log aggregometer (Model 592).

2.3.3. Platelet Activation. Fresh human platelet rich plasma (PRP) was centrifuged at 1000 *g* for 9 min. Washed platelets were prepared by resuspending the cell pellets in Hepes buffered modified Tyrode's solution (pH = 7.4).[68] X-*rdm*-DyOx aerogel samples (1 mg) were incubated with such washed platelet suspensions (50 μL) for up to 6 h at room temperature. Timed samples were taken at 2, 4, and 6 h and platelet activation was measured via platelet surface P-selectin (CD62P) expression, using a fluorescein isothiocyanate (FITC) conjugated monoclonal murine anti human CD62P antibody (252-040, Ancell Corp., Bayport, MN) in an Accuri C6 flow cytometer (BD Bioscience). Platelets processed similarly in the absence of aerogels served as controls.

2.3.4. Plasma C3a Level. X-*rdm*-DyOx aerogel-induced plasma anaphylatoxin C3a generation was measured using a C3a EIA kit (Quidel Corporation, Part No. A031). Normal PPP (50 μL) was incubated with X-*rdm*-DyOx discs (1 mg) for up to 24 h at 37 °C. Timed (at 2, 4, 6, and 24 h) samples (100 μL) were taken and 1 mM EDTA was added to stop complement activation. PPP samples were then diluted 1:100 v/v in the specimen diluent provided with the kit. Diluted samples and C3a standards were dispensed into a 96-well microtiter plate pre-coated with monoclonal murine anti human C3a antibody (1 h, RT). After it was washed, C3a conjugate (peroxidase conjugated rabbit anti human C3a antibody) was added to the wells to detect the captured C3a (1 h, RT). Antibody binding was detected using TMB substrate solution provided by the kit (3,3′,5,5′-tetramethylbenzidene and hydrogen peroxide). Color development was quantified with a BioTek ELX800 microplate reader (Fisher Scientific) at 450 nm, after the reaction was stopped with 1 N H_2SO_4. The C3a concentration was calculated using a standard curve. PPP without X-aerogel treatment was used as the control.

2.4. Aerogel Drug Loading Procedure. Loading of aerogels with paracetamol and indomethacin was carried out by placing monoliths in vials containing saturated ethanolic solutions of the drug for 24 h. (The solubility of paracetamol is 166 mg cm^{-3},[69] and of indomethacin is 6.5 mg cm^{-3}, both in ethanol.[70]) The volume of the drug solution was always 4× the volume of the monolith. Loading of insulin was carried out by placing the aerogel in an insulin solution (8 mg mL^{-1}) using an aqueous HCl solution (25 mM) as solvent. The vials were mildly agitated periodically. The monoliths were carefully taken out from the loading solutions and briefly dipped in fresh solvent to remove any excess of loosely bound surface adsorbed drug. Aerogels loaded with paracetamol and indomethacin were dried in a vacuum oven at 80 °C for 24 h, while aerogels loaded with insulin were freeze-dried.

2.5. Drug Release Procedure. Drug release rates were monitored either in phosphate buffer (pH = 7.4) or in 0.1 N aqueous HCl solution. For this, drug-loaded aerogel monoliths were pulverized with a Janke and Kunkel A-10 S1 laboratory grinder at 20 000 rpm for about 2 min to ≥125 μm particles, per manufacturer's specification. Aerogel powder (about 0.3 g) was introduced to the corresponding drug release medium (750 mL) in a 2 L round bottom flask at 37 °C, and the mixture was stirred continuously with a magnetic bar. Aliquots (2 mL) were taken at regular intervals, and the UV−vis absorption spectra were recorded. The drug concentrations were calculated using the absorbance at 245 nm for paracetamol, at 320 nm for indomethacin and at 270 nm for insulin. Typical data and calibration curves are shown in Appendix III of the Supporting Information. Each aliquot removed from the round bottom flask was replaced with the same amount of fresh drug release medium.

3. RESULTS AND DISCUSSION

3.1. Materials Synthesis and Biocompatibility. For reasons outlined in the Introduction, this drug storage and release study focuses on dysprosia aerogels, whose fragility has been addressed by a process referred to as crosslinking, whereas the skeletal framework is encapsulated under a nanothin polymer coating. The polymer here is polyurea formed *in situ* from Desmodur N3200 diisocyanate (see Experimental Section) reacting with the surface −OH groups and with gelation water remaining adsorbed on the oxide frameworks.[47,50,51,71−73] Those materials are referred to as X-*rdm*-DyOx, whereas "X-" refers to polymer crosslinking, "*rdm*" to the random arrangement of the porous structure and "DyOx" points to the fact that dysprosium oxide comprises the basis of the framework. The study was conducted comparatively with similar polyurea-crosslinked random silica aerogels denoted as X-*rdm*-SiOx,[50,51] which in turn were referenced to polyurea-crosslinked ordered mesoporous silica aerogels, X-*ord*-SiOx, which again were referenced to their native (non-crosslinked) samples (n-*ord*-SiOx).[52,53] Synthesis of all materials was based on literature procedures as outlined in the Experimental section and summarized in the flowcharts shown in Appendix I of the Supporting Information. Synthetic conditions were selected in order to match the bulk densities of X-*rdm*-DyOx and X-*rdm*-SiOx (0.437 g cm^{-3} and 0.517 g cm^{-3}, respectively), and to bracket those densities with n-*ord*-SiOx (0.304 g cm^{-3}) and X-*ord*-SiOx (0.75 g cm^{-3}). In terms of mechanical strength, the ultimate quasi-static compressive strength of X-*rdm*-DyOx (0.474 ± 0.002 g cm^{-3}), X-*rdm*-SiOx (0.478 ± 0.004 g cm^{-3}), and X-*ord*-SiOx (0.670 ± 0.003 g cm^{-3}) are quite high, as expected:[71,72] 375 ± 26 MPa, 186 ± 22 MPa,[51] and 804 ± 3 MPa,[52] respectively. The corresponding Young's moduli are 157 ± 12 MPa, 129 ± 8 MPa, and 274 ± 39 MPa, respectively. The underlying native random dysprosia (at 0.18 g cm^{-3}) was too weak to be tested. Native random silica (0.19 g cm^{-3}) on the other hand has a much lower ultimate compressive strength (4.05 ± 0.05 MPa), yet a fairly high Young's modulus (92 ± 7 MPa).[51]

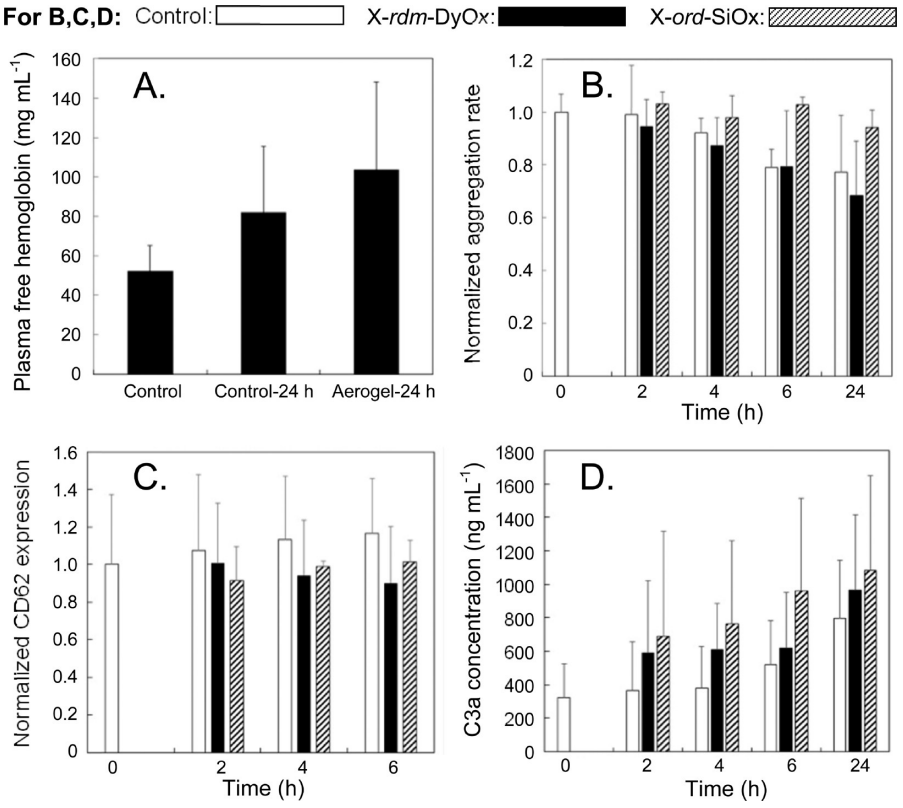

Figure 1. (A) Hemolysis test using X-*rdm*-DyOx via the free hemoglobin concentration in plasma (number of samples $n = 6$, Significance level, $P = 0.36$). (B) Platelet aggregation towards $TRAP_6$ ($n = 6$, $P > 0.06$). (C) Platelet activation via CD62P expression ($n = 6$, $P > 0.15$). (D) Immune response via plasma C3a concentration ($n = 4-5$, $P > 0.2$). All data are presented as mean + standard deviation. (Data for X-*ord*-SiOx, from ref 47.)

The ultimate compressive strength and Young's modulus of native ordered n-*ord*-SiOx made to match the densities of the X-*rdm*-silica and dysprosia samples (0.477 ± 0.004 g cm^{-3}) were measured at 17 ± 2 MPa (failed at 7.2% strain) and 205 ± 17 MPa, respectively. The overall behavior of all X- versus native samples is internally consistent, and has been interpreted as the elastic properties (Young's modulus) being controlled by the underlying inorganic skeletal framework, while the ultimate strength by the polymer coating.[51]

The biocompatibility of *X-rdm-DyOx* aerogels was evaluated via (a) a hemolysis test to determine whether aerogels cause damage to red blood cells (Figure 1A), (b) a platelet aggregation test towards $TRAP_6$ (thrombin receptor activator peptides) to investigate whether aerogels would affect platelet normal function, as for example their aggregation properties (Figure 1B), (c) a platelet activation test towards P-selectin (CD62P) expression to examine whether aerogels activate blood platelets, which could lead to thrombosis (Figure 1C), and (d) plasma anaphylatoxin C3a concentration measurements to determine whether aerogels would cause acute immune responses in plasma (Figure 1D). Experimental details are provided in the Experimental Section. For quick comparison, Figure 1 also includes data from X-*ord*-SiOx reported previously.[74−77] The hemolysis test showed that contact with X-*rdm*-DyOx did not cause any red blood cell damage. It is noted further that X-*rdm*-DyOx did not cause any significant changes in the normal platelet activation and aggregation, and on average the values were lower than both the control and X-*ord*-SiOx (Figure 1B and C). Incubation of fresh human platelet rich plasma (PPP) with X-*rdm*-DyOx for up to 24 h did not induce any significant increase in the anaphylatoxin C3a concentration indicating that X-*rdm*-DyOx do not cause a plasma acute immune response (Figure 1D). In fact, X-*rdm*-DyOx aerogels induced the lowest amount of C3a generation compared to all the other aerogels that have been tested in our laboratories.[78] The results of Figure 1 demonstrate that X-*rdm*-DyOx have acceptable biocompatibility, and therefore are viable candidates as drug delivery vehicles.

3.2. Characterization of the Nanostructure before Loading with Drug. The skeletal framework was characterized with electron microscopy. Figure 2A and C shows that both X-*rdm*-DyOx and X-*rdm*-SiOx consist of a random distribution of nanoparticles. X-*rdm*-DyOx seems to include larger interstitial pores, implying a more significant contribution of macroporosity (pore sizes >50 nm) to the pore structure. On the other hand, SEM (Figure 3A) shows that native n-*ord*-SiOx consists of large, micrometer-size particles, which are perforated by 7 nm diam. tubes in hexagonal packing (by TEM; Figure 3C). In polyurea-crosslinked X-*ord*-SiOx (Figure 3E), the surface of the micrometer-size particles has been smoothed out in SEM (compare Figure 3E with 3A), and their internal tubes have become almost invisible in TEM (Figure 3G), consistent with their being completely filled with polymer, as has been discussed extensively previously based on similar microscopic as well as x-ray diffraction data.[52,53]

The porosity, Π, was calculated from bulk and skeletal density data and a quantitative evaluation of the pore structure was obtained with N_2 sorption porosimetry (Table 1). X-*rdm*-DyOx aerogels are 69% porous, and their N_2 sorption isotherms rise at partial pressure $P/P_o > 0.9$ and show narrow hysteresis loops (Figure 4A), implying that X-*rdm*-DyOx are mainly macroporous materials with some degree of

Table 1. Materials Characterization Data of Aerogels Used for Drug Delivery

sample	linear shrinkage (%)[a,b]	bulk density, ρ_b (g cm^{-3})[a]	skeletal density, ρ_s (g cm^{-3})[c]	porosity, Π (% v/v)	specific pore volume (cm^3 g^{-1})[d]			BET surf. area, σ (m^2 g^{-1})	BJH plot max. (nm) [HWHM (nm)][e]	av. particle diam. (nm)[f]
					V_{Total}	$V_{1.7\text{-}300\_nm}$	$V_{>300\_nm}$			
X-*rdm*-DyOx	19	0.437 ± 0.008	1.394 ± 0.001	68.7 ± 0.6	1.571	0.474	1.097	48	74 [108]	90
X-*rdm*-SiOx	6	0.517 ± 0.008	1.321 ± 0.002	60.9 ± 0.6	1.177	0.684	0.493	169	12 [3]	27
X-*ord*-SiOx	10	0.750 ± 0.010	1.259 ± 0.003	40.4 ± 0.8	0.539	0.004	0.535	2		2383
n-*ord*-SiOx	23	0.304 ± 0.004	1.935 ± 0.004	84.3 ± 0.3	2.773	1.091	1.682	738	8 [1]	4

[a]Average of four samples. (Mold diameter = 1.05 cm.) [b]Shrinkage =100 × (mold diameter − sample diameter)/(mold diameter). [c]Single sample, average of 50 measurements. [d]V_{Total} was calculated via $V_{Total} = (1/\rho_b) - (1/\rho_s)$. $V_{1.7\_300\_nm}$ from the total N_2-desorption volume. $V_{>300\_nm} = V_{Total} - V_{1.7\_300\_nm}$. [e]From the desorption branch of the isotherm. First numbers are the peak maxima; numbers in brackets are the widths at half maxima. [f]By the $6/(\rho_s \times \sigma)$ method.

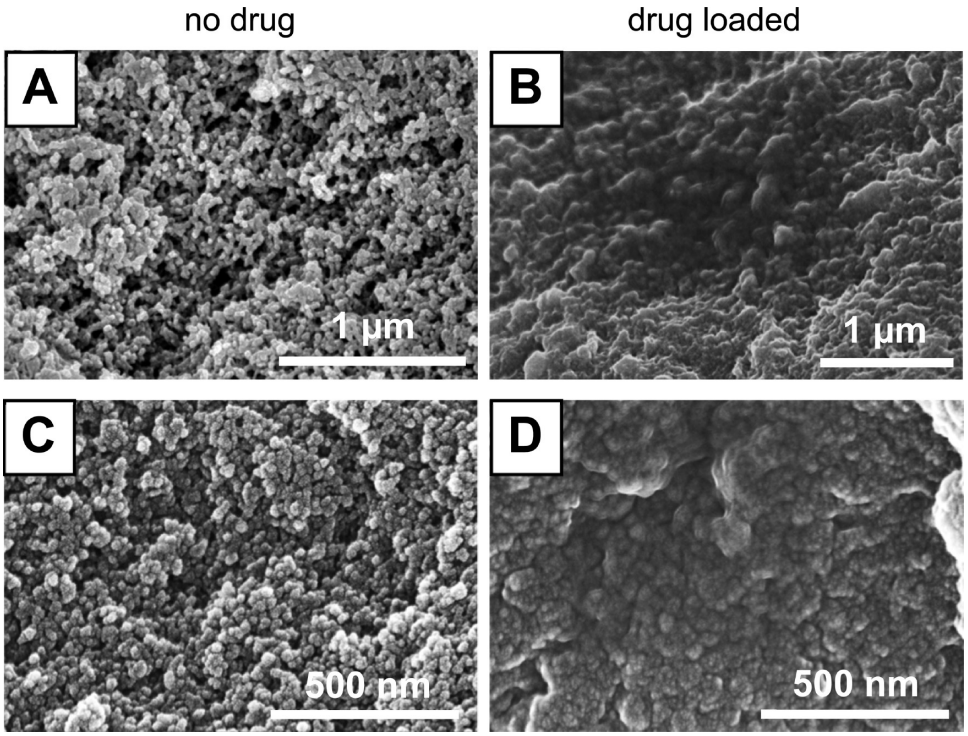

Figure 2. SEM using pulverized samples of (A) X-*rdm*-DyOx aerogel (ρ_b = 0.437 g cm^{-3}), (B) X-*rdm*-DyOx aerogel loaded with paracetamol, (C) X-*rdm*-SiOx aerogel (ρ_b = 0.517 g cm^{-3}), and (D) X-*rdm*-SiOx aerogel loaded with paracetamol.

mesoporosity. The pore size distribution using the Barrett−Joyner−Halenda (BJH) equation on the desorption branch of the isotherm is relatively broad (Figure 4A inset), and the pore volume allocated to pores sizes >300 nm is 2.3× that of pores in the 1.7−300 nm range ($V_{pores>300}/V_{pores\_1.7-300\_nm}$ = 2.3), confirming that X-*rdm*-DyOx are mostly macroporous materials. In contrast, the isotherms of X-*rdm*-SiOx (61% porous) start rising at P/P_o > 0.75 and reach well-defined saturation plateaus (Figure 4B); the pore size distribution is narrower (Figure 4B inset, average pore size, 12 nm) and the pore volume allocated to pore sizes in the 1.7−300 nm range is 1.3× that of pores with sizes >300 nm ($V_{pores>300}/V_{pores\_1.7-300\_nm}$ = 0.72), indicating that X-*rdm*-SiOx includes a significant amount of mesoporosity. Consequently, the BET surface area of X-*rdm*-SiOx (169 m^2 g^{-1}) is over 3× higher than that of X-*rdm*-DyOx aerogels (48 m^2 g^{-1}). The different pore structures of X-*rdm*-DyOx and X-*rdm*-SiOx reflect different particle sizes. Those have been calculated from BET surface area and skeletal density data (Table 1) and they are in agreement with the qualitative observations in SEM: 90 nm in X-*rdm*-DyOx and 27 nm in X-*rdm*-SiOx.

Consistent with SEM and TEM (Figures 3A and 3C), the isotherms of native ordered n-*ord*-SiOx (Figure 4C), reach broad saturation plateaus for mosty mesoporous materials. The pore size distribution is extremely narrow (Figure 4C inset) with an average pore size equal to 7 nm, matching the TEM data (Figure 3C). However, the pore volume corresponding to those pores is only 0.64× the pore volume of pores with sizes >300 nm ($V_{pores>300}/V_{pores\_1.7\text{-}300\_nm}$ = 1.54, data from Table 1) indicating that n-*ord*-SiOx is still a mostly macroporous material. On the other hand, although the shape of the isotherms of n-*ord*-SiOx aerogels are similar to those of crosslinked X-*rdm*-SiOx (Figure 4B), n-*ord*-SiOx is a mechanically weak material,[52,53] while X-*rdm*-SiOx is extremely strong.[50,51] As mentioned above, the mechanical strength of n-*ord*-SiOx was improved dramatically by polymer crosslinking,[52,53] but at the same time the isotherms of X-*ord*-SiOx show loss of all mesoporosity (Figure 4D) consistent with

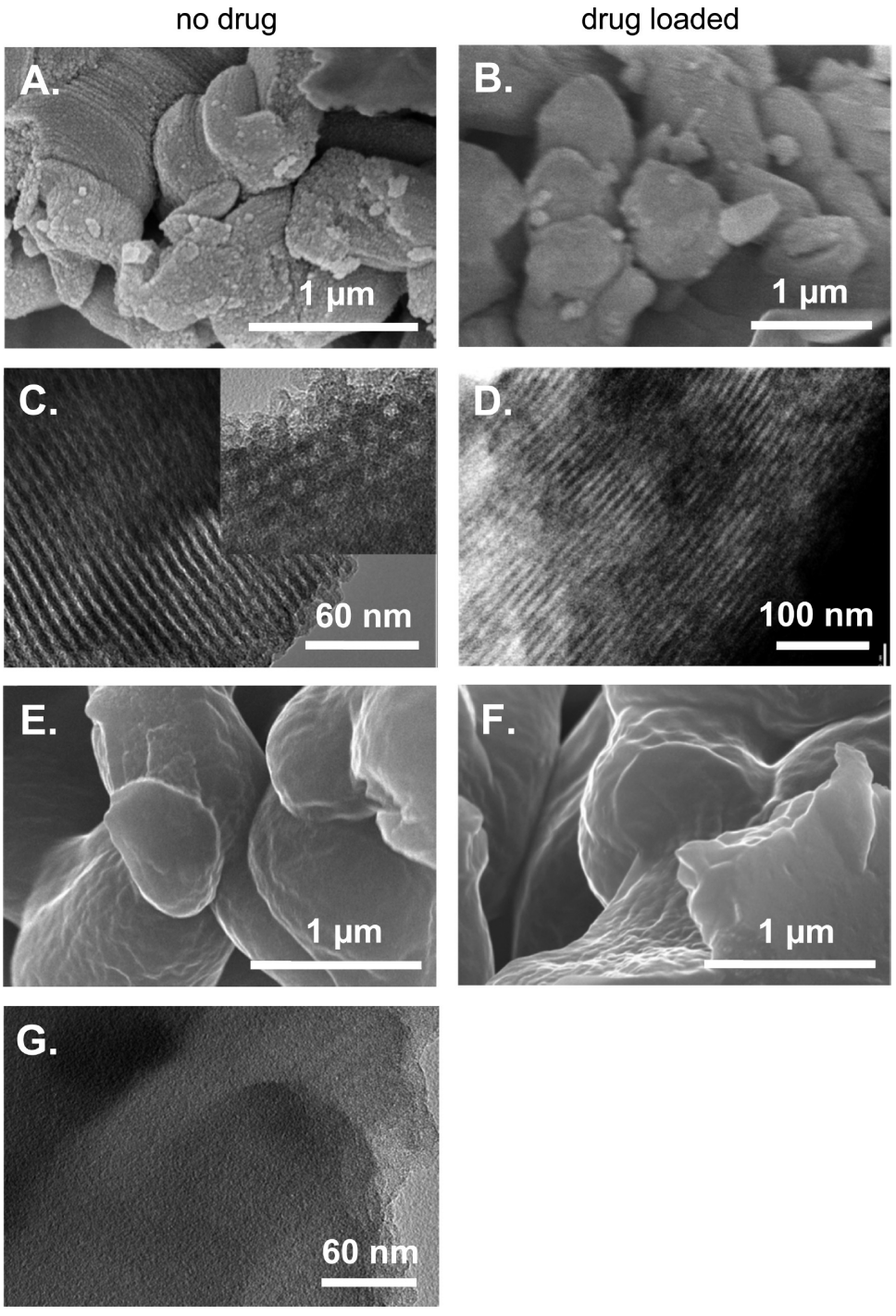

Figure 3. SEM using pulverized samples of (A) n-*ord*-SiOx aerogel (ρ_b = 0.304 g cm^{-3}), (B) n-*ord*-SiOx aerogel loaded with paracetamol, (C) TEM of n-*ord*-SiOx aerogel (inset shows top view of the periodic hexagonal tubes), (D) TEM of n-*ord*-SiOx aerogel loaded with paracetamol, (E) SEM of X-*ord*-SiOx aerogel (ρ_b = 0.750 g cm^{-3}), (F) SEM of X-*ord*-SiOx aerogel loaded with paracetamol, and (g) TEM of X-*ord*-SiOx aerogel.

polymer filling the tubular mesopores as discussed in relation to TEM above (Figure 3G). Consequently, the pore volume corresponding to pores with sizes in the 1.7−300 nm practically disappeared ($V_{pores>300}/V_{pores\_1.7\text{-}300\_nm}$>130), and the BET surface area decreased from 737 m^2 g^{-1} in n-*ord*-SiOx to a mere 2 m^2 g^{-1} in X-*ord*-SiOx. Clearly, the hexagonal tubes of n-*ord*-SiOx were no longer available for storing drug in X-*ord*-SiOx.

3.3. Drug Loading and Release. The intent of this study was to utilize the internal free volume (porosity) rather than the surface area of aerogels for storing drugs. To minimize drug adsorption at the artificial surfaces created by pulverization, and to ensure utilization only of the internal structure of the aerogels, drug loading was conducted with monoliths (rather than powders) using capillary forces to uptake saturated ethanolic solutions of paracetamol or indomethacin, or solutions of insulin in aqueous HCl. The solvent was removed either under vacuum at 80 °C (paracetamol and indomethacin), or by freeze-drying (insulin). Afterwards, dry drug-loaded monoliths were pulverized (see Experimental Section) and the amount of drug loading was quantified with thermogravimetric analysis in air (TGA). Representative TGA data are shown in

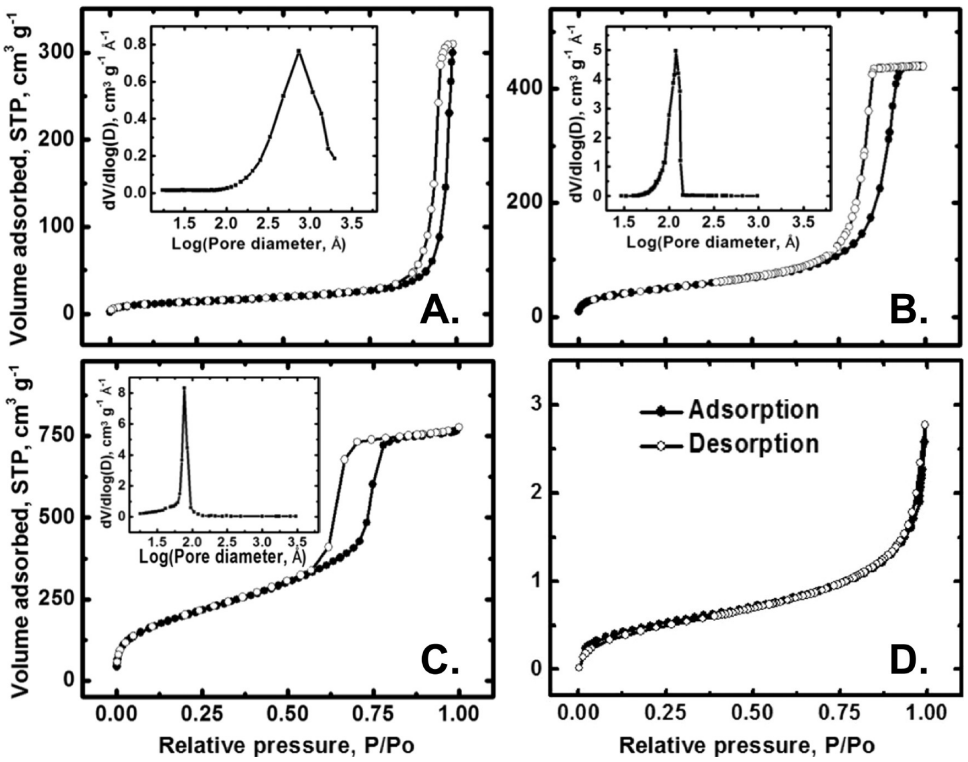

Figure 4. N_2 sorption isotherms of (A) X-*rdm*-DyOx aerogel (ρ_b = 0.437 g cm^{-3}), (B) X-*rdm*-SiOx aerogel (ρ_b = 0.517 g cm^{-3}), (C) n-*ord*-SiOx aerogel (ρ_b = 0.304 g cm^{-3}), and (D) X-*ord*-SiOx aerogel (ρ_b = 0.750 g cm^{-3}). Insets: BJH desorption plots.

Table 2. Percent Drug Loading of Aerogels from Thermogravimetric Analysis (TGA) Data

		percent drug loading					
aerogel	drug	% w/w	% w/v	volume of drug, V_{drug} (cm^3 g^{-1})[a]	volume of aerogel, V_a (cm^3 g^{-1})[b]	pore volume in V_a, V_{pore} (cm^3 g^{-1})[c]	percent of V_{pore} occupied by drug, Π_u (% v/v)[d]
X-*rdm*-DyOx	paracetamol	35 ± 1	15 ± 1	0.278 ± 0.008	1.487 ± 0.036	1.026 ± 0.036	27 ± 1
X-*rdm*-DyOx	indomethacin	33 ± 1	14 ± 1	0.250 ± 0.008	1.533 ± 0.036	1.058 ± 0.036	24 ± 1
X-*rdm*-DyOx	insulin	18 ± 3	8 ± 3	0.148 ± 0.025[e]	1.876 ± 0.077	1.295 ± 0.077	11 ± 2
X-*rdm*-SiOx	paracetamol	30 ± 1	16 ± 1	0.237 ± 0.008	1.354 ± 0.029	0.826 ± 0.029	29 ± 1
X-*ord*-SiOx	paracetamol	19 ± 1	14 ± 1	0.150 ± 0.008	1.080 ± 0.020	0.432 ± 0.020	35 ± 3
n-*ord*-SiOx	paracetamol	21 ± 2	6 ± 2	0.166 ± 0.016	2.599 ± 0.074	2.183 ± 0.074	8 ± 1
n-*ord*-SiOx	indomethacin	16 ± 1	5 ± 1	0.121 ± 0.008	2.763 ± 0.049	2.321 ± 0.049	5.0 ± 0.4

[a]Volume of drug in 1 g of drug-loaded aerogel, V_{drug} = (% of drug w/w)/(100 × ρ_{drug}) ($\rho_{drug}/\rho_{paracetamol}$ = 1.263 g cm^{-3}, $\rho_{indomethacin}$ = 1.320 g cm^{-3}). [b]Volume of aerogel, before drug loading, corresponding to 1 g of drug-loaded sample, V_a = [100 − (% of drug w/w)]/(100 × ρ_b) (ρ_b from Table 1). [c]V_{pore} = (V_a × Π)/100 (Π from Table 1). [d]Percent utilization of porosity for drug storage, Π_u = 100 × V_{drug}/V_{pore}. [e]Calculation based on $\rho_{insulin} \approx \rho_{proteins}$ = 1.22 g cm^{-3}.[79]

Figure S.1 of Appendix II of the Supporting Information. The percent weight of the respective drug was calculated from the difference in the terminal weights (at 800 °C) of aerogels samples before and after drug loading (see Appendix II of the Supporting Information). Percent weight data for the three drugs of this study are summarized in Table 2. Unfortunately, N_2 sorption porosimetry of drug-loaded samples was problematic, because drugs tend to leach out of the samples during measurement and contaminate the instrument. Therefore, the location of the drug on the skeletal framework was inferred from microscopy and by comparing drug-loading data for X-*rdm*-DyOx and the controls, as outlined below. For this, a useful parameter extracted from the gravimetric data (Table 2) in combination with (a) the density of the drugs, ρ_{drug}, and (b) the aerogel porosity (Π, from Table 1) is the percent porosity utilization (Π_u) for the drug storage, which is also included in Table 2.

Despite the large porosity reduction (from 84% to 40% v/v), and the much larger surface area reduction of ordered silica by polyurea crosslinking (from 738 m^2 g^{-1} in n-*ord*-SiOx to 2 m^2 g^{-1} in X-*ord*-SiOx), the amount of drug uptake remained about the same in the two kinds of samples (e.g., for paracetamol, 21 ± 2% and 19 ± 1% w/w, respectively). However, the percent porosity utilization, Π_u, of n-*ord*-SiOx for drug storage was only 8% v/v for paracetamol and 5% v/v for indomethacin, down from 35% v/v for X-*ord*-SiOx (Table 2). This suggests that the mesoporous space in the hexagonal tubes of ordered native n-*ord*-SiOx was not involved in the storage of the drug. Indeed, comparing the TEM images of n-*ord*-SiOx before and after drug loading (Figure 3C and D, respectively), with the TEM of X-*ord*-SiOx (whereas tubes have been filled with polyurea, Figure 3G), reveals that the ordered mesopores of n-*ord*-SiOx have the same size (7 nm) and appear open after drug uptake;

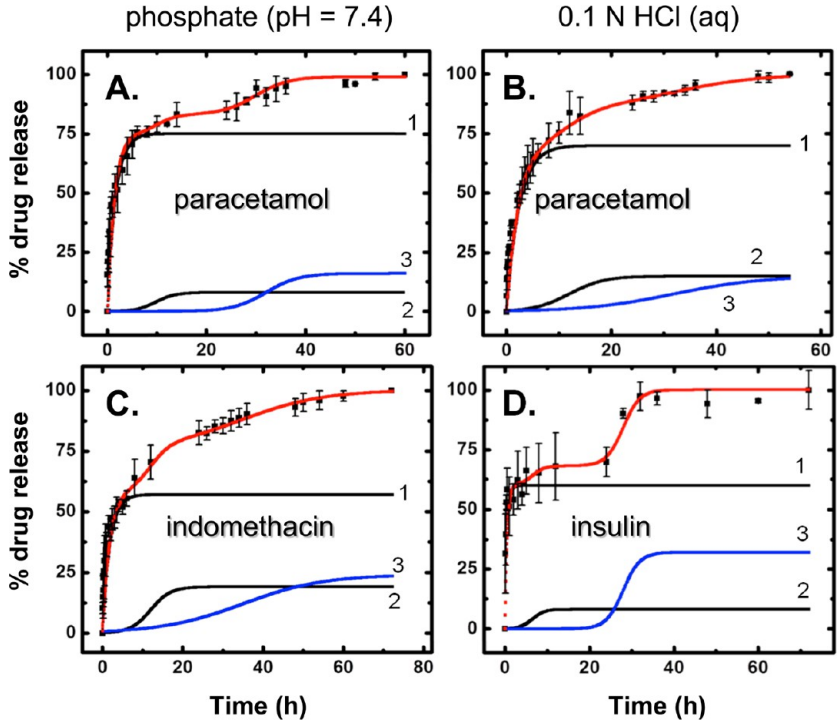

Figure 5. Drug release from drug loaded X-*rdm*-DyOx aerogel as a function of time as shown: (A) paracetamol in phosphate buffer (pH = 7.4), (B) paracetamol in 0.1 N aqueous HCl,; (C) indomethacin in phosphate buffer (pH = 7.4), and (D) insulin in 0.1 N aqueous HCl.

had those tubes been filled with organic matter (drug), their appearance in TEM should have been expected closer to that of X-*ord*-SiOx (Figure 3G). It is thus reasonable to conclude that drug clogs the entrance of the tubular mesopores, and remains confined in the macroporous space formed by the micrometer-size particles of all ordered silica samples. By the same token, while the general appearance (size, shape) of the micrometer-size particles of n-*ord*-SiOx remains the same after drug uptake (compare Figure 3E and F), SEM also shows that after drug loading the surface of those particles, which defines the macroporous space in n-*ord*-SiOx, is smoother (compare Figure 3B with A).

By SEM (Figure 2B and D), drug is uniformly distributed throughout both random X-*rdm*-DyOx and X-*rdm*-SiOx frameworks. In both materials the tiniest crevices between particles have been filled with new matter, which has spilled out and fills most of the macroporous space as well. The weight percent uptake of paracetamol or indomethacin by X-*rdm*-DyOx (33−35% w/w) was found in the same range with the value for X-*rdm*-SiOx (30% w/w), and higher than the uptake by ordered X-*ord*-SiOx (19% w/w); however, normalizing for the density difference between those samples, the volume percent uptake of the two drugs by X-*rdm*-DyOx (14−15% w/v) was equal to the uptake by all X-silicas, random and ordered: 14-16% w/v; refer to Table 2. (Insulin uptake by X-*rdm*-DyOx was lower (18% w/w or 8% w/v) owing to the lower concentration of that drug in the drug-loading solution.) The percent porosity utilization, Π_u, for drug storage in X-*rdm*-DyOx and X-*rdm*-SiOx reached 27-29% v/v, which is lower than the Π_u values of X-*ord*-SiOx (35% v/v), but higher than that of n-*ord*-SiOx (5-8% v/v). Although in terms of porosity utilization X-*ord*-SiOx seems to have a slight advantage over X-*rdm*-SiOx and X-*rdm*-DyOx, on the other hand the porosity of X-*ord*-SiOx (40% v/v) is lower than that of random samples (61-69% v/v). Therefore, X-*rdm*-SiOx and X-*rdm*-DyOx have an edge in terms of their weight percent ability to store drug. However, this *static* quantification is only one side of the coin. The other one concerns the *dynamic* behavior of drug-loaded aerogels under drug release conditions. The capacity to store drug is a necessary condition for considering a porous material as a drug delivery system, but it is not sufficient alone: a slow release profile is equally important.

Drug release rates were studied spectrophotometrically. For this, the entire spectrum of the drug-release medium was recorded in regular time intervals (t), thus ensuring also absence of degradation by processing or by the long interaction of the drug with the aerogel matrix. Typical data along with the calibration curves are shown in Figure S.2 of Appendix III of the Supporting Information. Release of paracetamol was monitored in both phosphate buffer (pH = 7.4), and 0.1 N aqueous HCl, while release of indomethacin, which, as a carboxylic acid, is practically insoluble in acidic media (the solubility of indomethacin at pH = 1.2 is just 3.882 μg mL^{-1}), was monitored only in phosphate buffer. Release of insulin was studied in 0.1 N aqueous HCl solution. Drug release data from X-*rdm*-DyOx are shown in Figure 5, and from the silica controls in Figure 6. Data for all samples were fitted with eq 1, which

$$\%\ \text{drug release} = \underset{\text{curve 1}}{A_1[1 - \exp[C_1(B_1 - t)]]} + \underset{\text{curve 2}}{\frac{A_2}{[1 + \exp[C_2(B_2 - t)]]}} + \underset{\text{curve 3}}{\frac{A_3}{[1 + \exp[C_3(B_3 - t)]]}} \quad (1)$$

includes an exponential term (denoted as curve 1) and two sigmoidal components (curves 2 and 3). The individual curves 1−3 are included and marked specifically in both Figures 5 and 6. The corresponding coefficients A_i, B_i, and C_i ($1 \le i \le 3$) are listed in Table 3. The contribution of each component is quantified through A_i, the position of each curve in time (t) is quantified by coefficients B_i and the time constant of the release (i.e., how sharp

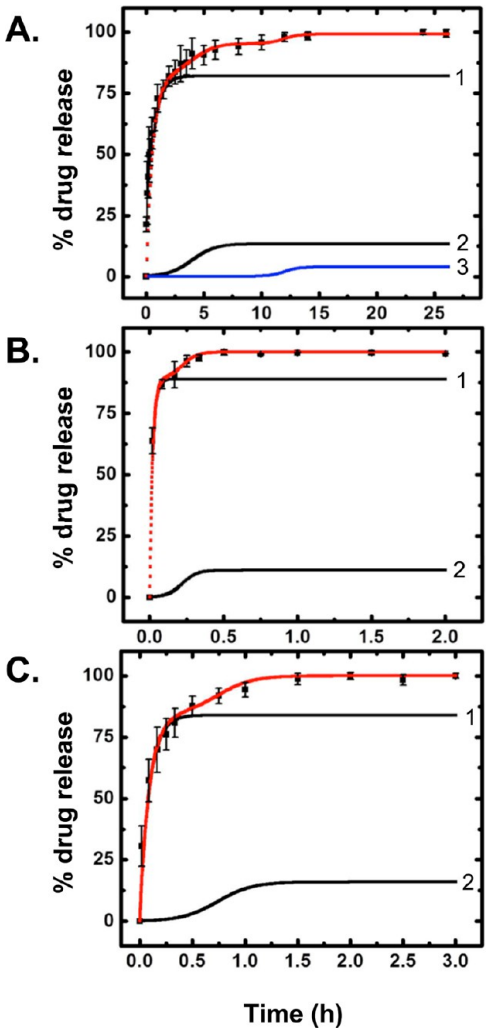

Figure 6. Paracetamol release in phosphate buffer (pH = 7.4) from various drug-loaded silica aerogels: (A) X-*rdm*-SiOx, (B) n-*ord*-SiOx, and (C) X-*ord*-SiOx.

or protracted the release is) is quantified by coefficients C_i. Thus, the sum of coefficients A_i is equal to 100% as expected, by definition $B_1 < B_2 < B_3$, and drug release is sharper for $C_i > 1$ and more protracted for $C_i < 1$. Interestingly, for all samples $B_1 = 0$ and $A_1 > A_2$, A_3, meaning that in all drug-loaded aerogels the largest portion of the drug was held loosely and was released faster starting from the moment the sample was placed in the release medium.

Two further observations are also immediately apparent: (a) drug release from randomly porous X-*rdm*-DyOx and X-*rdm*-SiOx (Figures 5 and 6A, respectively) takes much longer than release from ordered silica; and (b) fitting of drug release from the random mesoporous samples requires all three terms of eq 1, while fitting of drug release from ordered samples, native or crosslinked (Figure 6B and C, respectively) can be accomplished with only two terms (curve 1 and curve 2).

The three terms of eq 1 are analogous to electrochemical equations that describe convective-diffusion driven flux (faradaic current) of redox active substances, whereas different amounts of material (A_i) diffuse from a solid surface into a semi-infinite medium, in which bulk concentration conditions are brought and maintained close to the solid surface (within <1 mm) by convection (stirring). In analogy to the standard redox potential, B_i describes the sequence of events, and C_i describes how facile or sluggish the process is (kinetics).[80] Thus, curve 1 addresses unobstructed escape of material plated onto to a substrate (e.g., analogous to the dissolution of a metal),[81] while curves 2 and 3 describe situations where the escaping material is in microscopic equilibrium with another form of itself (e.g., in the electrochemical analogue, two redox forms in electron transfer equilibrium with an electrode). Considering those inferences together with the hierarchical porous nanostructure of randomly porous aerogels,[82] a reasonable model for the drug storage and release from random silica and dysprosia is described in Scheme 1, whereas drug filling "deeper" pores is "protected" by drug confined on the outer surfaces that define the macroporous space, and therefore is released later. More protracted release, (lower C_i values), is attributed to (a) the strength of the interactions within the confined mesoporous space and (b) the solubility of the drug in the release medium. The interactions within the mesoporous space are attributed to hydrogen (H) bonding of the drug with itself and with the −NH−C(═O)−NH− groups of the polyurea coating over the silica or dysprosia frameworks. Hence, by keeping the release medium constant (phosphate buffer), indomethacin, with more functional groups capable of developing H-bonding (especially note the −COOH group) shows a more protracted release from the innermost locations in the framework, than release of paracetamol (compare curves marked "3" in Figure 5A and C, and note $C_{3,\text{indomethacin}} = 0.1\ h^{-1}$ versus $C_{3,\text{paracetamol}} = 0.3\ h^{-1}$ in Table 3). On the other hand, as stated above, the solubility of indomethacin in 0.1 M aqueous HCl is very low; thus, working with paracetamol only, its release in acid is protracted relative to phosphate buffer (compare Figure 5A and B), probably owing to the lower

Table 3. Drug Release Data Analysis According to Eq 1[a]

			curve 1			curve 2			curve 3			
sample	drug	drug release medium	A_1	B_1	C_1	A_2	B_2	C_2	A_3	B_3	C_3	$A_1 + A_2 + A_3$
X-*rdm*-DyOx	paracetamol	phosphate, pH 7.4	75	0	0.71	8	10.0	0.50	16	32	0.30	99
X-*rdm*-DyOx	paracetamol	0.1 N HCl (aq)	70	0	0.42	15	12.0	0.30	15	32	0.12	100
X-*rdm*-DyOx	indomethacin	phosphate, pH 7.4	57	0	0.56	19	12.0	0.40	24	35	0.10	100
X-*rdm*-DyOx	insulin	0.1 N HCl (aq)	60	0	2.00	8	6.50	0.70	32	28	0.50	100
X-*rdm*-SiOx	paracetamol	phosphate, pH 7.4	82	0	1.72	13	4.00	1.00	4	12	1.50	99
X-*ord*-SiOx	paracetamol	phosphate, pH 7.4	84	0	11.1	16	0.74	6.00	*b*	*b*	*b*	100
n-*ord*-SiOx	paracetamol	phosphate, pH 7.4	89	0	50.0	11	0.22	20.0	*b*	*b*	*b*	100
n-*ord*-SiOx	paracetamol	0.1 N HCl (aq)	87	0	50.0	11	0.18	22.0	*b*	*b*	*b*	98
n-*ord*-SiOx	indomethacin	phosphate, pH 7.4	87	0	33.3	13	0.27	14.0	*b*	*b*	*b*	100

[a] A_i = dimensionless % w/w of drug in the particular site (i); B_i in h, C_i in h^{-1} ($1 \le i \le 3$). [b] Data could be fitted with only two terms in eq 1.

dx.doi.org/10.1021/am4059217 | ACS Appl. Mater. Interfaces 2014, 6, 4891−4902

Scheme 1. Location of Drugs within the Hierarchical Porous Structure of Random X-*rdm*-DyOx or X-*rdm*-SiOx[a]

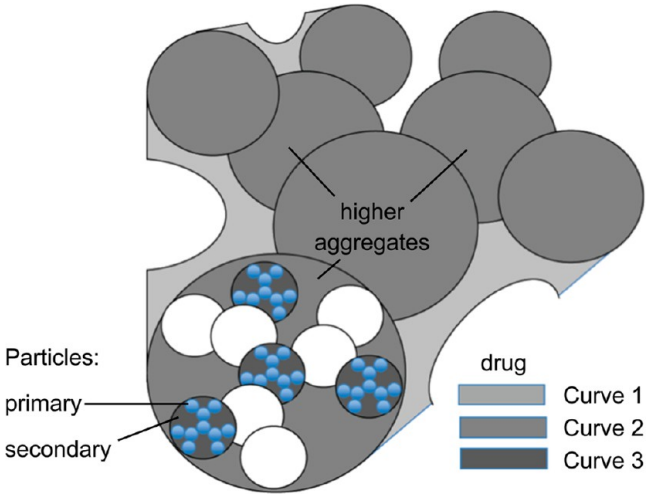

[a]For clarity, several secondary particles have been left open; internal structure is shown only for one higher aggregate of secondary particles. Drug released from different shaded areas gives rise to curves 1−3 in Figures 5 and 6A.

solubility expected from a phenol in an acidic environment. Insulin is stable only in acidic media and its release (Figure 5D) follows a similar pattern to that of paracetamol at pH = 7.4 (Figure 5A).

Consistent with this model, strong H-bonding of paracetamol with itself as well as with the hydroxyl groups at the narrow (7 nm) entrance of the long tubes of native n-*ord*-SiOx leads to accumulation that blocks access to the interior of the pores, hence further drug accumulation takes place only on the large particles that define the macropores. In that regard, drug release from n-*ord*-SiOx (Figure 6B) is quite similar to that from X-*ord*-SiOx (Figure 6C), in which the pores are filled completely with polyurea. (It is noted that polyurea is formed within the tubular mesopores, because transport of the non-hydrogen-bonding isocyanate monomer is unobstructed.) The slower component (B_2) in both n- and X-*ord*-SiOx is attributed to drug released from the (still macroporous) crevices between the large particles in Figures 3B and 3F, respectively, while the faster drug release from n-*ord*-SiOx (50% release in about 1 min, complete release in about 1 h) than from X-*ord*-SiOx (50% release in about 3.5 min, complete release in about 2 h) is attributed to the breakdown and disintegration of the internal structure defined by the large particles in Figure 3, caused by capillary forces upon submersion in the drug-release medium.

4. CONCLUSION

Dysprosia is an inexpensive non-toxic material, therefore a reasonable candidate for biomedical applications. In that context, here dysprosia aerogels were investigated comparatively to silica aerogels as drug delivery systems. For this, the entire skeletal framework of all materials was coated (crosslinked) with polyurea, which provides mechanical strength and prevents peptization. After biocompatibility was established, the most important finding of this study was a correlation of the drug release profile with the nested hierarchical porous structure: innermost stored drug is buried underneath, protected by and released more slowly than more loosely held drug in outer macropores. In that regard, ordered mesoporosity (in the form of long, narrow (7 nm) tubes in hexagonal packing) does not comprise an advantage either in the ability of the material to store drug, or in the drug release profile: selected model drugs pursued here clog the ends of the hexagonal tubes, so that their internal space becomes irrelevant as far as drug storage is concerned. Thus, the drug release profile from native open-mesoporous silica (n-*ord*-SiOx) has shown only two levels of drug storage and was almost identical to the drug release profile from its crosslinked counterpart (X-*ord*-SiOx) whereas the pores have been filled with polymer. Consistent with that finding, there was no significant advantage of polymer-crosslinked random dysprosia aerogels (X-*rdm*-DyOx) over the analogous silica samples (X-*rdm*-SiOx), both showing three levels available for drug storage. Nevertheless, considering several additional attributes of dysprosia (e.g., high magnetic susceptibility and possibility for neutron activation) provides X-*rdm*-DyOx with a multifunctionality edge over silica worth pursuing further.

■ ASSOCIATED CONTENT

Supporting Information

Appendix I containing flow charts for the aerogel synthetic protocols, appendix II containing TGA data and calculation method for the weight percent of drug loading, and appendix III containing typical spectrophotometric data for drug release. This information is available free of charge via the Internet at http://pubs.acs.org.

■ AUTHOR INFORMATION

Corresponding Authors

*E-mail: leventis@mst.edu (N.L.).
*E-mail: cslevent@mst.edu (C.S.-L.).

Notes

The authors declare no competing financial interest.

■ ACKNOWLEDGMENTS

This project was initiated with funding from the National Science Foundation (NSF-DMR-0907291) and was supported by the Army Research Office under Award Number W911NF-10-1-0476. We thank Bayer Corporation, U.S.A. for their generous supply of Desmodur N3200, and the Materials Research Center of MS&T for support with materials characterization (SEM, TEM).

■ REFERENCES

(1) Lu, X.; Feng, L.; Akasaka, T.; Nagase, S. Current Status and Future Developments of Endohedral Metallofullerenes. *Chem. Soc. Rev.* **2012**, *41*, 7723−7760.

(2) Lacerda, L.; Bianco, A.; Prato, M.; Kostarelos, K. Carbon Nanotubes as Nanomedicines: From Toxicology to Pharmacology. *Adv. Drug Delivery Rev.* **2006**, *58*, 1460−1470.

(3) Torchilin, V. P. Multifunctional Nanocarriers. *Adv. Drug Delivery Rev.* **2006**, *58*, 1532.

(4) Vogelson, C. T. Advances in Drug Delivery Systems. *Mod. Drug Discovery* **2001**, *4*, 49−52.

(5) Farokhzad, O. C.; Langer, R. Impact of Nanotechnology on Drug Delivery. *ACS Nano* **2009**, *3*, 16−20.

(6) Bangham, A. D.; Standish, M. M.; Watkins, J. C. Diffusion of Univalent Ions across the Lamellae of Swollen Phospholipids. *J. Mol. Biol.* **1965**, *13*, 238−252.

(7) Farokhzad, O. C.; Langer, R. Nanomedicine: Developing Smarter Therapeutic and Diagnostic Modalities. *Adv. Drug Delivery Rev.* **2006**, *58*, 1456−1459.

(8) Wagner, V.; Dullaart, A.; Bock, A.-K.; Zweck, A. The Emerging Nanomedicine Landscape. *Nat. Biotechnol.* **2006**, *24*, 1211−1217.
(9) Ng, V. W. K.; Berti, R.; Lesage, F.; Kakkar, A. Gold: A Versatile Tool for In Vivo Imaging. *J. Mater. Chem. B* **2013**, *1*, 9−25.
(10) Raemdonck, K.; Demeester, J.; Smedt, S. D. Advanced Nanogel Engineering for Drug Delivery. *Soft Matter* **2009**, *5*, 707−715.
(11) Bhattarai, N.; Gunn, J.; Zhang, M. Chitosan-Based Hydrogels for Controlled, Localized Drug Delivery. *Adv. Drug Delivery Rev.* **2010**, *62*, 83−99.
(12) Szymanski, P.; Magdalena, M.; Mikiciuk-Olasik, E. Nanotechnology in Pharmaceutical and Biomedical Applications. Dendrimers. *Nano* **2011**, *6*, 509−539.
(13) Lin, Q.; Jiang, G.; Tong, K. Dendrimers in Drug-Delivery Applications. *Des. Monomers Polym.* **2010**, *13*, 301−324.
(14) Kamaly, N.; Xiao, Z.; Valencia, P. M.; Radovic-Moreno, A. F.; Farokhzad, O. F. Targeted Polymeric Therapeutic Nanoparticles: Design, Development and Clinical Translation. *Chem. Soc. Rev.* **2012**, *41*, 2971−3010.
(15) Figuerola, A.; Corato, R. D.; Manna, L.; Pellegrino, T. From Iron Oxide Nanoparticles Towards Advanced Iron-based Inorganic Materials Designed for Biomedical Applications. *Pharmacol. Res.* **2010**, *62*, 126−143.
(16) Cole, A. J.; Yang, V. C.; David, A. E. Cancer Theranostics: The Rise of Targeted Magnetic Nanoparticles. *Trends Biotechnol.* **2011**, *29*, 323−332.
(17) Pierre, A. C.; Pajonk, G. M. Chemistry of Aerogels and Their Applications. *Chem. Rev.* **2002**, *102*, 4243−4265.
(18) Colilla, M.; Gonzalez, B.; Vallet-Regi, M. Mesoporous Silica Nanoparticles for the Design of Smart Delivery Nanodevices. *Biomater. Sci.* **2013**, *1*, 114−134.
(19) Guenther, U.; Smirnova, I.; Neubert, R. H. H. Hydrophilic Silica Aerogels as Dermal Drug Delivery Systems −Dithranol as a Model Drug. *Eur. J. Pharm. Biopharm.* **2008**, *69*, 935−942.
(20) Vallet-Regi, M.; Ramila, A.; del Real, R. P.; Perez-Pariente, J. A New Property of MCM-41: Drug Delivery System. *Chem. Mater.* **2001**, *13*, 308−311.
(21) Doadrio, A. L.; Sousa, E. M. B.; Doadrio, J. C.; Perez-Pariente, J.; Izquierdo-Barba, I.; Vallet-Regi, M. Mesoporous SBA-15 HPLC Evaluation for Controlled Gentamicin Drug Delivery. *J. Controlled Release* **2004**, *97*, 125−132.
(22) Song, S.-W.; Hidajat, K.; Kawi, S. Functionalized SBA-15 Materials as Carriers for Controlled Drug Delivery: Influence of Surface Properties on Matrix-Drug Interactions. *Langmuir* **2005**, *21*, 9568−9575.
(23) Smirnova, I.; Mamic, J.; Arlt, W. J. Adsorption of Drugs on Silica Aerogels. *Langmuir* **2003**, *19*, 8521−8525.
(24) Rolison, D. R. Catalytic Nanoarchitectures: The Importance of Nothing and the Unimportance of Periodicity. *Science* **2003**, *299*, 1698−1701.
(25) Vallet-Regi, M. Ordered Mesoporous Materials in the Context of Drug Delivery Systems and Bone Tissue Engineering. *Chem.—Eur. J.* **2006**, *12*, 5934−5943.
(26) Manzano, M.; Vallet-Regi, M. New Developments in Ordered Mesoporous Materials for Drug Delivery. *J. Mater. Chem.* **2010**, *20*, 5593−5604.
(27) Mal, N. K.; Fujiwara, M.; Tanaka, Y. Photocontrolled Reversible Release of Guest Molecules from Coumarin-Modified Mesoporous Silica. *Nature* **2003**, *421*, 350−353.
(28) Lai, J.; Mu, X.; Xu, Y.; Wu, X.; Wu, C.; Li, C.; Chen, J.; Zhao, Y. Light-Responsive Nanogated Ensemble based on Polymer Grafted Mesoporous Silica Hybrid Nanoparticles. *Chem. Commun.* **2010**, *46*, 7370−7372.
(29) Knezevic, N. Z.; Trewyn, B. G.; Lin, V. S. Y. Functionalized Mesoporous Silica Nanoparticle-Based Visible Light Responsive Controlled Release Delivery System. *Chem. Commun.* **2011**, *47*, 2817−2819.
(30) Schlossbauer, A.; Warncke, S.; Gramlich, P. M. E.; Kecht, J.; Manetto, A.; Carell, T.; Bein, T. A Programmable DNA-Based Molecular Valve for Colloidal Mesoporous Silica. *Angew. Chem., Int. Ed.* **2010**, *49*, 4734−4737.
(31) Du, L.; Liao, S.; Khatib, H. A.; Stoddart, J. F.; Zink, J. I. Controlled-Access Hollow Mechanized Silica Nanocontainers. *J. Am. Chem. Soc.* **2009**, *131*, 15136−15142.
(32) Zhao, Y.-L.; Li, Z.; Kabehie, S.; Botros, Y. Y.; Stoddart, J. F.; Zink, J. I. pH-Operated Nanopistons on the Surfaces of Mesoporous Silica Nanoparticles. *J. Am. Chem. Soc.* **2010**, *132*, 13016−13025.
(33) Gan, Q.; Lu, X.; Yuan, Y.; Qian, J.; Zhou, H.; Lu, X.; Shi, J.; Liu, C. A Magnetic, Reversible pH-responsive Nanogated Ensemble Based on Fe_3O_4 Nanoparticles-Capped Mesoporous Silica. *Biomaterials* **2011**, *32*, 1932−1942.
(34) Chen, P.-J.; Hu, S.-H.; Hsiao, C.-S.; Chen, Y.-Y.; Liu, D.-M.; Chen, S.-Y. Multifunctional Magnetically Removable Nanogated Lids of Fe_3O_4-Capped Mesoporous Silica Nanoparticles for Intracellular Controlled Release and MR Imaging. *J. Mater. Chem.* **2011**, *21*, 2535−2543.
(35) Ruiz-Hernández, E.; Baeza, A.; Vallet-Regi, M. Smart Drug Delivery through DNA/Magnetic Nanoparticle Gates. *ACS Nano* **2011**, *5*, 1259−1266.
(36) Smirnova, I.; Suttiruengwong, S.; Arlt, W. J. Feasibility Study of Hydrophilic and Hydrophobic Silica Aerogels as Drug Delivery Systems. *J. Non-Cryst. Solids* **2004**, *350*, 54−60.
(37) Rosenholm, J. M.; Linden, M. Towards Establishing Structure−Activity Relationships for Mesoporous Silica in Drug Delivery Applications. *J. Controlled Release* **2008**, *128*, 157−164.
(38) Alnaief, M.; Smirnova, I. Effect of Surface Functionalization of Silica Aerogel on their Adsorptive and Release Properties. *J. Non-Cryst. Solids* **2010**, *356*, 1644−1649.
(39) Hudson, S. P.; Padera, R. F.; Langer, R.; Kohane, D. S. The Biocompatibility of Mesoporous Silicates. *Biomaterials* **2008**, *29*, 4045−4055.
(40) Fontecave, T.; Sanchez, C.; Azais, T.; Boissiere, C. Chemical Modification as a Versatile Tool for Tuning Stability of Silica Based Mesoporous Carriers in Biologically Relevant Conditions. *Chem. Mater.* **2012**, *24*, 4326−4336.
(41) Wu, S.-H.; Lin, C.-Y.; Hung, Y.; Chen, W.; Chang, C.; Mou, C.-Y. PEGylated Silica Nanoparticles Encapsulating Multiple Magnetite Nanocrystals for High-performance Microscopic Magnetic Resonance Angiography. *J. Biomed. Mater. Res. B* **2011**, *99B*, 81−88.
(42) Lin, I.-C.; Liang, M.; Liu, T.-Y.; Jia, Z.; Monteiro, M. J.; Toth, I. Effect of Polymer Grafting Density on Silica Nanoparticle Toxicity. *Biorg. Med. Chem.* **2012**, *20*, 6862−6869.
(43) Mehling, T.; Smirnova, I.; Guenther, U.; Neubert, R. H. H. Polysaccharide-Based Aerogels As Drug Carriers. *J. Non-Cryst. Solids* **2009**, *355*, 2472−2479.
(44) Garcia-Gonzalez, C. A.; Alnaief, M.; Smirnova, I. Polysaccharide-Based Aerogels—Promising Biodegradable Carriers for Drug Delivery Systems. *Carbohydr. Polym.* **2011**, *86*, 1425−1438.
(45) Gaudio, P. D.; Auriemma, G.; Mencherini, T.; Porta, G. D.; Reverchon, E.; Aquino, R. P. Design of Alginate-Based Aerogel for Nonsteroidal Anti-Inflammatory Drugs Controlled Delivery Systems Using Prilling and Supercritical-Assisted Drying. *J. Pharm. Sci.* **2013**, *102*, 185−194.
(46) Lethal dose of dysprosium oxide >5 g kg^{-1}: www.nfc.umn.edu/assets/pdf/msds/dysprosium_oxide.pdf (accessed 11/21/2013).
(47) Leventis, N.; Vassilaras, P.; Fabrizio, E. F.; Dass, A. Polymer Nanoencapsulated Rare Earth Aerogels: Chemically Complex but Stoichiometrically Similar Core−Shell Superstructures with Skeletal Properties of Pure Compounds. *J. Mater. Chem.* **2007**, *17*, 1502−1508.
(48) Buzea, C.; Pacheco, I. I.; Robbie, K. *Biointerphases* **2007**, *2*, No. MR-17-MR71.
(49) Medina, C.; Santos-Martinez, M. J.; Radomski, A.; Corrigon, O. I.; Radomski, M. W. *Brit. J. Pharmacol.* **2007**, *150*, 552−558.
(50) Meador, M. A. B.; Capadona, L. A.; McCorkle, L.; Papadopoulos, D. S.; Leventis, N. Structure−Property Relationships in Porous 3D Nanostructures as a Function of Preparation Conditions: Isocyanate Cross-Linked Silica Aerogels. *Chem. Mater.* **2007**, *19*, 2247−2260.

(51) Katti, A.; Shimpi, N.; Roy, S.; Lu, H.; Fabrizio, E. F.; Dass, A.; Capadona, L. A.; Leventis, N. Chemical, Physical, and Mechanical Characterization of Isocyanate Cross-Linked Amine-Modified Silica Aerogels. *Chem. Mater.* **2006**, *18*, 285−296.
(52) Leventis, N.; Mulik, S.; Wang, X.; Dass, A.; Patil, V. U.; Sotiriou-Leventis, C.; Lu, H.; Churu, G.; Capecelatro, A. Polymer Nano-Encapsulation of Templated Mesoporous Silica Monoliths with Improved Mechanical Properties. *J. Non-Cryst. Solids* **2008**, *354*, 632−644.
(53) Leventis, N.; Mulik, S.; Wang, X.; Dass, A.; Sotiriou-Leventis, C.; Lu, H. Stresses at the Interface of Micro with Nano. *J. Am. Chem. Soc.* **2007**, *129*, 10660−10661.
(54) Lacheisserie, E. d. T. d.; Gignoux, D.; Schlenker, M. *Magnetism: Fundamentals*, 1st ed.; Springer: New York, 2004.
(55) Sole, J. G.; Bausa, L.; Jaque, D. *An Introduction to the Optical Spectroscopy of Inorganic Solids*, 1st ed.; John Wiley & Sons Ltd.: Chichester, U.K., 2005.
(56) Wang, A. Z.; Bagalkot, V.; Vasilliou, C. C.; Gu, F.; Alexis, F.; Zhang, L.; Shaikh, M.; Yuet, K.; Cima, M. J.; Langer, R.; Kantoff, P. W.; Bander, N. H.; Jon, S.; Farokhzad, O. C. Superparamagnetic Iron Oxide Nanoparticle−Aptamer Bioconjugates for Combined Prostate Cancer Imaging and Therapy. *Chem. Med. Chem.* **2008**, 3, 1311−1315.
(57) Gomaa, M. A.; Mohamed, E. J. Neutron Detection Using Dy_2O_3 Activation Detectors. *Radiat. Phys. Chem.* **1979**, *13*, 41−43.
(58) Sledge, C. B.; Noble, J.; Hnatowich, D. J.; Kramer, R.; Shortkroff, S. Experimental Radiation Synovectomy by ^{165}Dy Ferric Hydroxide Macroaggregate. *Arthritis Rheum.* **1977**, *20*, 1334−1342.
(59) Cacaina, D.; Areva, S.; Laaksonen, H.; Simon, S.; Ylanen, H. Preparation and Complex Characterization of Silica Holmium Sol−Gel Monoliths. *J. Mater. Sci.: Mater. Med.* **2011**, *22*, 29−40.
(60) White, J. E.; Day, D. E.; Brown, R. F.; Ehrhardt, G. J. Biodegradable Rare Earth Lithium Aluminoborate Glasses for Brachytherapy Use. *Ceram. Eng. Sci. Proc. III* **2010**, *31*, 3−17.
(61) Zuckerman, J. D.; Sledge, C. B.; Shortkroff, S.; Venkatesan, P. Treatment of Rhuematoid Arthritis using Radiopharmaceuticals. *Nucl. Med. Biol.* **1987**, *14*, 211−218.
(62) Zhao, D.; Yu, J.; Huang, W.; Zhou, N.; Wang, D.; Yin, W.; Chen, Y. Dysprosium Lithium Borate Glass Microspheres for Radiation Synovectomy: The *In Vitro* and *In Vivo* Performance Evaluation. *Mater. Sci. Eng. C* **2010**, *30*, 970−974.
(63) Laurin, C. A.; Desmarchais, J.; Daziano, L.; Gariepy, R.; Derome, A. Long-Term Results of Synovectomy of the Knee in Rheumatoid Patients. *J. Bone Joint Surg. Am.* **1974**, *56-A*, 521−531.
(64) Conzone, S. D.; Brown, R. F.; Day, D. E.; Ehrhardt, G. J. *In Vitro* and I*n Vivo* Dissolution Behavior of a Dysprosium Lithium Borate Glass Designed for the Radiation Synovectomy Treatment of Rheumatoid Arthritis. *J. Biomed Mat. Res.* **2002**, *60*, 260−268.
(65) Leventis, N.; Sotiriou-Leventis, C.; Chandrasekaran, N.; Mulik, S.; Larimore, Z. J.; Lu, H.; Churu, G.; Mang, J. T. Multifunctional Polyurea Aerogels from Isocyanates and Water. A Structure−Property Case Study. *Chem. Mater.* **2010**, *22*, 6692−6710.
(66) Amatani, T.; Nakanishi, K.; Hirao, K.; Kodaira, T. Monolithic Periodic Mesoporous Silica with Well-Defined Macropores. *Chem. Mater.* **2005**, *17*, 2114−2119.
(67) Yin, W.; Ngwe, E. C.; Rubenstein, D. A. A Biocompatible Flow Chamber to Study the Hemodynamic Performance of Prosthetic Heart Valves. *ASAIO J.* **2012**, *58*, 470−480.
(68) Yin, W.; Ghebrehiwet, B.; Peerschke, E. I. Expression of Complement Components and Inhibitors on Platelet Microparticles. *Platelets* **2008**, *19*, 225−233.
(69) Granberg, R. A.; Rasmuson, A. C. Solubility of Paracetamol in Pure Solvents. *J. Chem. Eng. Data* **1999**, *44*, 1391−1395.
(70) https://www.caymanchem.com/app/template/Product.vm/catalog/70270 (accessed 11/21/2013).
(71) Leventis, N.; Sotiriou-Leventis, C.; Zhang, G.; Rawashdeh, A.-M. M. Nanoengineering Strong Silica Aerogels. *Nano Lett.* **2002**, *2*, 957−960.
(72) Leventis, N. Three-Dimensional Core-Shell Superstructures: Mechanically Strong Aerogels. *Acc. Chem. Res.* **2007**, *40*, 874−884.
(73) Leventis, N.; Sotiriou-Leventis, C.; Mulik, S.; Dass, A.; Schnobrich, J.; Hobbs, A.; Fabrizio, E. F.; Luo, H.; Churu, G.; Zhang, Y.; Lu, H. Polymer Nanoencapsulated Mesoporous Vanadia with Unusual Ductility at Cryogenic Temperatures. *J. Mater. Chem.* **2008**, *18*, 2475−2482.
(74) Yin, W.; Venkitachalam, S. M.; Jarrett, E.; Staggs, S.; Leventis, N.; Lu, H.; Rubenstein, D. A. Biocompatibility of Surfactant-Templated Polyurea−Nanoencapsulated Macroporous Silica Aerogels with Plasma Platelets and Endothelial Cells. *J. Biomed. Mater. Res. A* **2010**, *92*, 1431−1439.
(75) Rubenstein, D. A.; Lu, H.; Mahadik, S. S.; Leventis, N.; Yin, W. Characterization of the Physical Properties and Biocompatibility of Polybenzoxazine-Based Aerogels for Use as a Novel Hard-Tissue Scaffold. *J. Biomater. Sci., Polym. Ed.* **2012**, *23*, 1171−1184.
(76) Sabri, F.; Sebelik, M. E.; Meacham, R.; Boughter, J. D., Jr.; Challis, M. J.; Leventis, N. *In Vivo* Ultrasonic Detection of Polyurea Crosslinked Silica Aerogel Implants. *PloS one* **2013**, *8*, e66348.
(77) Sabri, F.; Boughter, J. D., Jr.; Gerth, D.; Skalli, O.; Phung, T. C.; Tamula, G. R.; Leventis, N. Histological Evaluation of the Biocompatibility of Polyurea Crosslinked Silica Aerogel Implants in a Rat Model: A Pilot Study. *PloS One* **2012**, *7*, No. e50686.
(78) Yin, W.; Lu, H.; Leventis, N.; Rubenstein, D. A. Characterization of the Biocompatibility and Mechanical Properties of Polyurea Organic Aerogels with the Vascular System: Potential as a Blood Implantable Material. *Int. J. Polym. Mater.* **2013**, *62*, 109−118.
(79) Quillin, M. L.; Matthews, B. W. Accurate calculation of the density of proteins. *Acta Crystallogr., D* **2000**, *56*, 791−794.
(80) Bard, A. J.; Faulkner, L. J. *Electrochemical Methods, Fundamentals and Applications*, 2nd ed.; Wiley: New York, 2000; Chapter 1.
(81) Bard, A. J.; Faulkner, L. J. *Electrochemical Methods, Fundamentals and Applications*, 2nd ed.; Wiley: New York, 2000; Chapter 1, p 33.
(82) Mohite, D. P.; Larimore, Z. J.; Lu, H.; Mang, J. T.; Sotiriou-Leventis, C.; Leventis, N. Monolithic Hierarchical Fractal Assemblies of Silica Nanoparticles Cross-Linked with Polynorbornene via ROMP: A Structure−Property Correlation from Molecular to Bulk through Nano. *Chem. Mater.* **2012**, *24*, 3434−3448.